Effect of gas diffusion layer properties on water distribution across air-cooled, open-cathode polymer electrolyte fuel cells: a combination of *ex-situ* X-ray tomography and *in-situ* neutron imaging.

Quentin Meyer[1], Sean Ashton[2], Pierre Boillat[3,4], Magali Cochet[3], Erik Engebretsen[1], Rhodri Jervis[1], Xuekun Lu[1], Donal P. Finegan[1], Joshua Bailey[1], Rema Abdulaziz[1], Noramalina Mansor[1], Dami Taiwo[1], Sergio Torija[2], Simon Foster[2], Paul Adcock[2], Paul R. Shearing[*1], Dan J. L. Brett[*1]

[1]Electrochemical Innovation Lab, Department of Chemical Engineering, UCL, London, WC1E 7JE, United Kingdom.

[2]Intelligent Energy, Charnwood Building Holywell Park, Ashby Road, Loughborough Leicestershire, LE11 3GB, United Kingdom.

[3]Electrochemistry Laboratory (LEC), Paul Scherrer Institute (PSI), 5232 Villigen, Switzerland.

[4]Neutron Imaging and Activation Group (NIAG), Paul Scherrer Institute (PSI), 5232 Villigen, Switzerland.

* Author to whom correspondence should be addressed
Tel.: +44(0)20 7679 3310
Web: www.ucl.ac.uk/electrochemical-innovation-lab
Email: d.brett@ucl.ac.uk; p.shearing@ucl.ac.uk

Highlights

- First description of in-plane water distribution using neutron imaging in an air-cooled, open-cathode fuel cell.
- High water content identified under cathode land area, whereas anode water content is relatively homogeneous.
- Water distribution in anode GDL directly linked to dispersion of PTFE.
- Anode GDL composition shown to affect water content and distribution in cathode.
- Combined X-ray computed tomography, SEM/EDS and TGA used to characterise GDL structure and composition.

Abstract

In-situ diagnostic techniques provide a means of understanding the internal workings of fuel cells under normal operating conditions so that improved designs and operating regimes can be identified. Here, an approach is used which combines *ex-situ* characterisation of two anode gas diffusion / microporous layers (GDL-A and GDL-B) with X-ray computed tomography and *in-situ* analysis using neutron imaging of operating fuel cells. The combination of TGA, SEM and X-ray computed tomography reveals that GDL-A has a thin microporous layer with ~26 % PTFE covering a thick diffusion layer composed of 'spaghetti' shaped fibres. GDL-B is covered by two microporous media (29 % and 6.5 % PTFE) penetrating deep within the linear fibre network. The neutron imaging reveals two pathways for water management underneath the cooling channel, either diffusing through the cathode GDL to the active channels, or diffusing through the membrane and towards the

anode. Here, these two behaviours are directly affected by the anode gas diffusion PTFE content and porosity.

Keywords

1.1. Introduction

Polymer electrolyte fuel cells (PEFC) fuelled with hydrogen are among the most promising energy conversion technologies for a broad range of applications, including portable, stationary and automotive power delivery. However, understanding the cell water management is crucial for performance optimisation. Flooding impedes reactant transport (water mainly concentrating at the cathode) and reduces the surface area of the catalyst, causing significant if not catastrophic decay in cell performance, and dehydration can lead to cracks and irreversible damage [1–3]. The gas diffusion layer (GDL) provides a pathway for electron transport, ensures even reactant delivery and helps water management within each cell. The water balance between flooding and membrane dehydration is a function of the GDL's structure, porosity and PTFE (hydrophobic) content. Here, two commercial GDLs with microporous layers are characterised *ex-situ* by capturing the design and structure via X-ray computed tomography (CT), along with its polytetrafluoroethylene (PTFE) / carbon distribution via SEM/EDS analysis and thermogravimetric analysis (TGA); *in-situ* 'visualisation' of the water distribution in the in-plane orientation was performed using neutron radiography. These techniques can be correlated with one another to gain new insights into the water management role of the GDL in fuel cells.

1.2. Gas diffusion layers

Gas diffusion layers [4], located between bipolar plates and catalyst layers, need to act as effective current conductors, yet be porous enough to provide a pathway to promote gas flow distribution to the catalyst layer and act to expel water to prevent electrode flooding [5]. Therefore, the structure of the GDL, fibre geometry and porosity [6], as well as applied compression [7] have been under investigation to understand how to optimise gas and water transport without hindering electron transport. Engineering of the material has been of particular focus, as its structure and PTFE content directly affect the water management and fuel cell performance [3,8–10]. The GDL is usually composed of carbon fibres around 5-10 μm in diameter, coated with a PTFE/carbon medium 'microporous' layer [11]. The most suitable concentration of PTFE within the GDL [8,12,13] and MPL [14] is of particular focus, as it regulates water accumulation and polymer electrolyte humidification [13].

To understand and optimize the transport phenomena through these porous materials, it is necessary to study the microstructural characteristics using high resolution techniques. Until recently, the main technique used to determine the GDL structure was scanning electron microscopy (SEM), frequently coupled with energy dispersive X-ray spectroscopy (EDS) analysis. SEM is useful in obtaining surface structural data, layer thickness, 'smoothness' of different interfaces, PTFE bonding, and fibre orientation, but fails to reveal the porosity and internal structure [5,6,15–22]. Micro and nano X-ray computed tomography (CT) are non-destructive methods that can achieve sufficiently high resolution for the imaging of carbon fibres, which typically have diameters between 5 and 10 μm, and they have been increasingly used to characterise GDLs [7,19,23–26]. Unlike SEM, computed tomography can be used to capture the internal 3D structure, and through image processing techniques, can help determine the porosity, pore size and tortuosity. Thermogravimetric analysis (TGA) has been used to quantify PTFE content [8,27,28] in the gas diffusion layer. The pyrolysis process provides the mass of PTFE in the entire sample analysed, whereas SEM / EDS provides an indication of the surface PTFE content.

4

1.3. Water visualisation in fuel cells

Neutron imaging can identify water in the in-plane orientation (with the membrane plane parallel to the beam) and in the through-plane orientation (with the membrane plane perpendicular to the beam). In the first case, it is possible to differentiate between the water content in the cathode and the anode GDL [29–36]. In the second case, it enables investigations of the effect of different designs, components, and operating conditions on the water distribution across the lateral extent of the cell [37–47]. Neutron imaging has been combined with other modelling and experimental techniques, such as current mapping [48], computational fluid dynamics (CFD) model validation [34,49,50], optical imaging [51], neutron scattering [52] and localised electrochemical impedance spectroscopy (EIS) [53]. The authors have recently combined neutron imaging with current and temperature mapping in a single device [37,38], linking water formation / evaporation with current density and temperature under steady state and transient conditions.

1.4. Air-cooled, Open-Cathode Fuel Cells

Unlike conventional closed-cathode fuel cells, self-breathing fuel cells offer the advantages of simpler design and integration into systems, using diffusion from the atmosphere without compressors. Passive air-breathing systems are typically limited to a maximum current density of ~0.6 A cm^{-2} [54–58] due to heat and water management issues, since water cannot be removed from the membrane, except through evaporation [56,59]. In the so-called 'air-cooled, open-cathode' configuration, air is forced through the cathode channels using fans, which improves performance and enables higher current densities to be attained [60–64] (Figure 1).

2. Experimental

2.1. Material

Fuel cell testing

Two 2-cell (60 cm^2 active area) air-cooled / air-breathing fuel cell stacks were used for testing (Intelligent Energy Ltd., UK). The membrane electrode assembly was composed of commercially available GDLs, membranes and electrodes with platinum loadings of 0.1 and 0.4 mg cm^{-2} on the anode and cathode, respectively. In this study, two stacks are compared (Stack-A and Stack-B), with the only difference being the anode GDL (Figure 1). The test station supplied dry hydrogen (with a purity of 99.995 %) at ambient temperature to the anodes and air was forced through the stack by a single fan (SanAce 36, Sanyo Denki, Japan) to the open-cathode channels [65]. The fan, which provides cooling and air supply to the cathode, was controlled by a programmable power supply (3649A Agilent, UK), and installed on top of an aluminium air funnel (Figure 1). The current drawn from the PEFC was controlled using an electronic load (PLZ664WA, Kikusui, Japan) in galvanostatic mode. An in-house computer-controlled system controlled the air, hydrogen, cooling and electrical valves (LabVIEW, National Instruments, USA) as well as recording and presenting data using a data acquisition card (USB 6363, National Instruments, USA). Ambient temperature, pressure (absolute) and relative humidity (RH) were measured at 25 °C $\pm$ 0.2 °C, 0.97 $\pm$ 0.02 bar and 40 %, respectively, during all tests. The operation of this fuel cell in terms of cathode design, cooling and active channels and materials, has been described in previous reports, and is summarised in Figure 1 [65,66]. The cathode is operated in flow-through mode, with an air flow rate of 1 × 10^{-3} m^3 s^{-1}. The exhaust hydrogen flow rate in through-flow mode was measured using a thermal mass flow meter (MassVIEW, Bronkhorst, UK) to be 4.7 SLPM, which corresponds to a stoichiometric ratio of 2 at 1 A cm^{-2}.
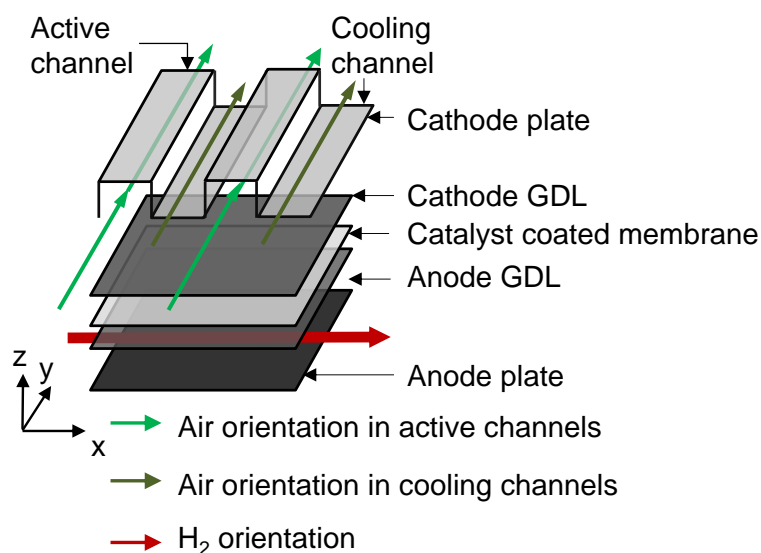
Figure 1. Illustration of the entire cell, showing the air and hydrogen orientation, along with the active and cooling channels of the cathode (not to scale). Hydrogen flows laterally through the anode GDL from inlet to outlet.

2.2. Characterisation methods.

Thermogravimetric analysis (TGA).

TGA was used to determine the PTFE mass content in GDL-A and GDL-B. The weight loss as a function of temperature was determined by thermogravimetric analysis (TGA) using a Pyris™ 1 TGA (PerkinElmer, USA), in a furnace with a sensitivity of 0.1 μg. The samples were heated in N_2, between 50 and 900 $^{\circ}$C, with a heating rate of 20 $^{\circ}$Cmin^{-1} and had an initial weight of 5.36 mg and 4.02 mg for GDL-A and GDL-B, respectively.

Scanning electron microscopy (SEM) with energy dispersive X-ray spectroscopy (EDS) analysis.

The GDLs for SEM imaging were cut into samples of diameters 2 mm and attached onto carbon adhesive disks. The samples were gold-coated for SEM to increase electronic conductivity and reduce the potential for charging-related artefacts. These

7

samples were investigated using the EVO MA 10 (Carl Zeiss, USA). SEM micrographs were taken of the cross-section and longitudinal (top and bottom) sections of each GDL. At low magnification, an electron accelerating voltage of 10-20 kV and the use of a lateral secondary electron detector enabled the imaging of both fibres and the microporous medium with a pixel resolution of ~700 nm in cross-section and between a pixel resolution of 500 nm and 50 nm in longitudinal section.

Quantification of the PTFE content from EDS images.

The EDS maps of the longitudinal sections of each GDL were used to quantify the fluorine (F) and carbon (C) mass content, since the quantity of fluorine is a useful metric for determining the PTFE, $(C_2F_4)_n$, content, upon subtraction of the gold signal. As PTFE is composed of 24 wt% C (molar mass $M_F = 12$ g mol^{-1}), and 76 wt% F (molar mass $M_F = 19$ g mol^{-1}), using the measured fluorine mass, it is possible to calculate the mass of PTFE ($m_{PTFE} = 1.31$ m_F, $m_{pure\ carbon} = m_{C,PTFE}$-0.31 m_F, with $m_{C,PTFE}$ referring to the carbon contained in the PTFE molecule). The penetration depth at 20 kV is <1 μm, therefore the assumption is made that each material imaged is homogeneous [67]. The analysis was conducted over six sample areas for each element for statistical relevance. Residual carbon contamination from the environment was neglected and care was taken to minimise this effect. The carbon adhesive disks do not affect the measurements, due to the EDS low penetration depth.

X-ray computed tomography

For each GDL, samples of diameter 3 mm were mounted on a 1 cm diameter SEM stage. These samples were investigated using a laboratory X-ray computed tomography system, Xradia VERSA 520 (Carl Zeiss, USA). The voxel size was ~1.46 μm for both samples. For each sample, a sequence of 1601 radiographs were collected over 4 hours, with an exposure time of 8 s and a source voltage of 30 kV,

resulting in a voxel size of ~1.46 μm; consequently the field-of-view is 0.5 × 0.5 mm. The radiographs were then reconstructed using Xradia XMReconstructor software.

Image post-processing

For all scans, post-processing and image segmentation was performed using FEI Avizo® to segment the GDL layer material, consisting of large fibres, from the microporous medium. The microporous medium is made of carbon/PTFE, and therefore its grayscale value is similar to that of the fibres. Therefore, a texture-based built-in segmentation technique (i.e. white top hat) together with morphological operations (i.e. opening and closing) were used to separate the fibres and the microporous medium as the fibres are highly oriented compared with carbon/PTFE. Due to the limited resolution of the scan (1.46 μm) determined by sample size, field-of-view and signal-to-noise ratio, the exact porosity could not be accurately determined spatially due to the microporous layer mostly consisting of features in the region of 5-10 nm. Consequently, regions were defined as high, low or medium porosity based on visual inspection. This is supported by SEM images which capture more accurately the microporous features.

Neutron imaging

Neutron radiography was performed at the neutron imaging facility NEUTRA of the SINQ spallation source (Paul Scherrer Institute, Switzerland) [68]. Thermal neutrons provided by the source are extracted from a moderator tank in the thermal energy range of 1 × 10^{-3} to 10 eV with a Maxwellian spectrum energy of 25 × 10^{-3} eV. In order to image the water distribution across the cell materials, the cell faced the neutron beam in the in-plane orientation (*xz*) (Figure 2). The detector consists of a neutron-sensitive LiF/ZnS scintillator and a charge-coupled CCD device (Ikon-L, Andor) camera housed in a light-tight box (Figure 2). The neutron beam is converted

into a photonic field by the scintillator, whereby the intensity of evoked light is proportional to the intensity of the incoming neutron beam [68].
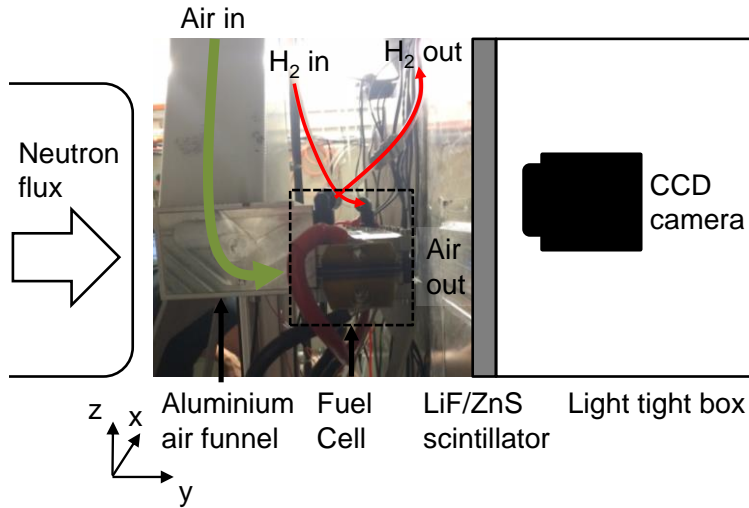

Figure 2. Illustration of neutron imaging arrangement with fuel cell facing the LiF/ZnS scintillator for in-plane measurements in NEUTRA [68]; air and hydrogen feed orientation shown.

Quantification of the water thickness from neutron images.

All the materials contribute to the attenuation of the neutron beam. In order to determine the attenuation due to the water only, one must start by making a certain number of corrections and divide all images by a reference image of the dry fuel cell. Then, since the attenuation of water follows the Beer-Lambert law, the water thickness can be extracted using Equation 1.

$$ I/I_0 = \exp(-\mu_{water} t_{water}) \tag{1} $$

With I the intensity of the beam in operation, I_o the intensity of the beam for the dry cell (without water), μ_{water} the attenuation coefficient of water, t_{water} the thickness of water. I and I_o are determined after all necessary corrections (filtering, subtraction of background components, alignment of 'working' and reference images) [69].

The water thickness is then extracted by taking the logarithm, divided by the attenuation coefficient μ_{water}.

$$t_{water} = -\frac{\ln\left({I}/{I_o}\right)}{\mu_{water}} \qquad (2)$$

In our case, μ_{water}, the attenuation coefficient of neutrons in liquid water, was measured in the NEUTRA beamline for the given setup at 3.5 cm^{-1} [40]. In the following sections, the water content is expressed as the 'effective water thickness' t_{water} in μm. In the in-plane orientation, a pixel resolution of 16.5 μm is obtained in the z-axis and 100 μm in the x-axis.

3. Results

3.1. Gas diffusion layer characterisation

Characterisation of the GDLs includes TGA to validate the PTFE content, and SEM/EDS coupled with X-ray computed tomography, to image the structure and determine the composition of each layer.

3.1.1. Thermogravimetric analysis

The two GDLs were characterised using TGA to determine their PTFE content (Figure 3). The analysis was performed in nitrogen to separate carbon from the other materials contained within the GDL. No significant decay in mass was observed below 300 ^{o}C. A mass drop was observed at 550 ^{o}C, which corresponds to the pyrolysis of PTFE [70,71]. GDL-A contains 5 wt%, whereas GDL-B contains 15 wt%. Although the carbon does not combust, it may corrode during the production of

PTFE decomposition products during the pyrolysis (CO_2, hydrocarbons, benzene), which may explains the linear decay above 600 ^{o}C [28,71,72].
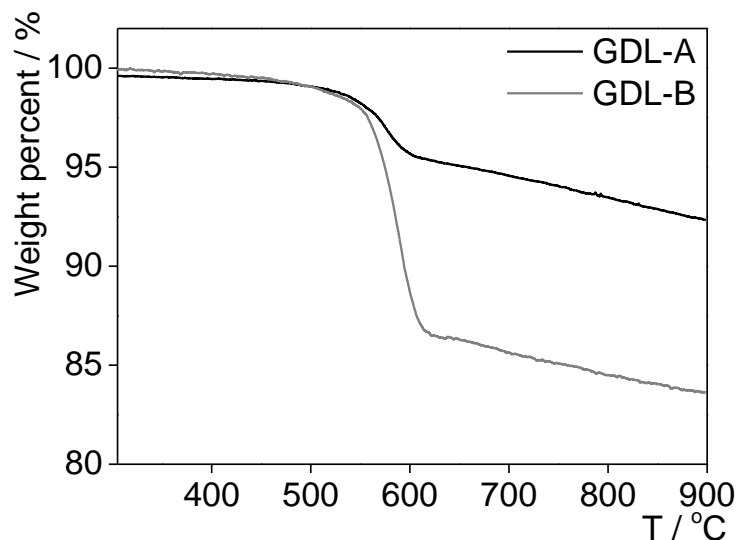

Figure 3. TGA analysis of GDL-A and GDL-B in nitrogen for a heating rate of 20 ^{o}C min^{-1}.

3.1.2. Microstructural characterisation

An approach similar to that of Pfrang *et al.* [26] was applied here, using SEM to gain insight into the surface microstructure before discriminating the 3D structure of the microporous layer and fibres using X-ray computed tomography (CT). Three SEM images are shown for each GDL-A and GDL-B sample: from the top (microporous layer side), bottom (fibre side) and along the cross-section. By coupling this analysis with X-ray CT, comprehensive structural information can be obtained (Figure 4).

In GDL-A, a single microporous layer A_1 can be observed, in GDL-B, two mediums have been deposited, B_1 and B_2. The structure of each was determined using SEM and X-ray CT and EDS was used to determine the PTFE content at the surface of the samples (Figure 4, Table 1). The X-ray CT orthoslices show a different density of

features for the MPL between the microporous medium A_1, B_1 and B_2, shown in Figure 4, and the large fibres in GDL-A and GDL-B.

GDL-A has a total thickness of 210 μm. It is composed of high porosity (volume fraction: 0.3) curved carbon fibres, which primarily run in the plane of the GDL. Similar structures are found in commercial GDLs, such as SIGRACET GDLs AA and AB, and Freudenberg FCCT [21]. On top of the GDL fibres is the microporous medium A_1 (~60 μm), with low porosity composed of ~26 wt% PTFE. There is a smooth planar interface between the MPL and GDL fibres, with an intrusion depth of the microporous layer into the GDL (fibre region) of less than two fibre thicknesses (~25 μm) (Figure 4 a).

GDL-B has an uneven thickness over the sample scanned (250-290 μm). It is composed of planar linear fibres of high porosity (volume fraction: 0.074). Similar structures are typically found for Toray and SolviCore GDLs [21]. Two microporous media, B_1 and B_2, are bound to the fibres, with low porosity for B_1 and medium porosity for B_2; they intrude substantially into the GDL material (Figure 4b). B_1 has a high PTFE content of ~29 wt%, whereas B_2 is lower at ~6.5 wt%. This creates a material composition gradient across the sample. The structure of GDL-B is similar to the commercial EP40 T0 (AvCarb, USA), with a graphitized resin binder mixed with PTFE deposited on the large fibres [17].
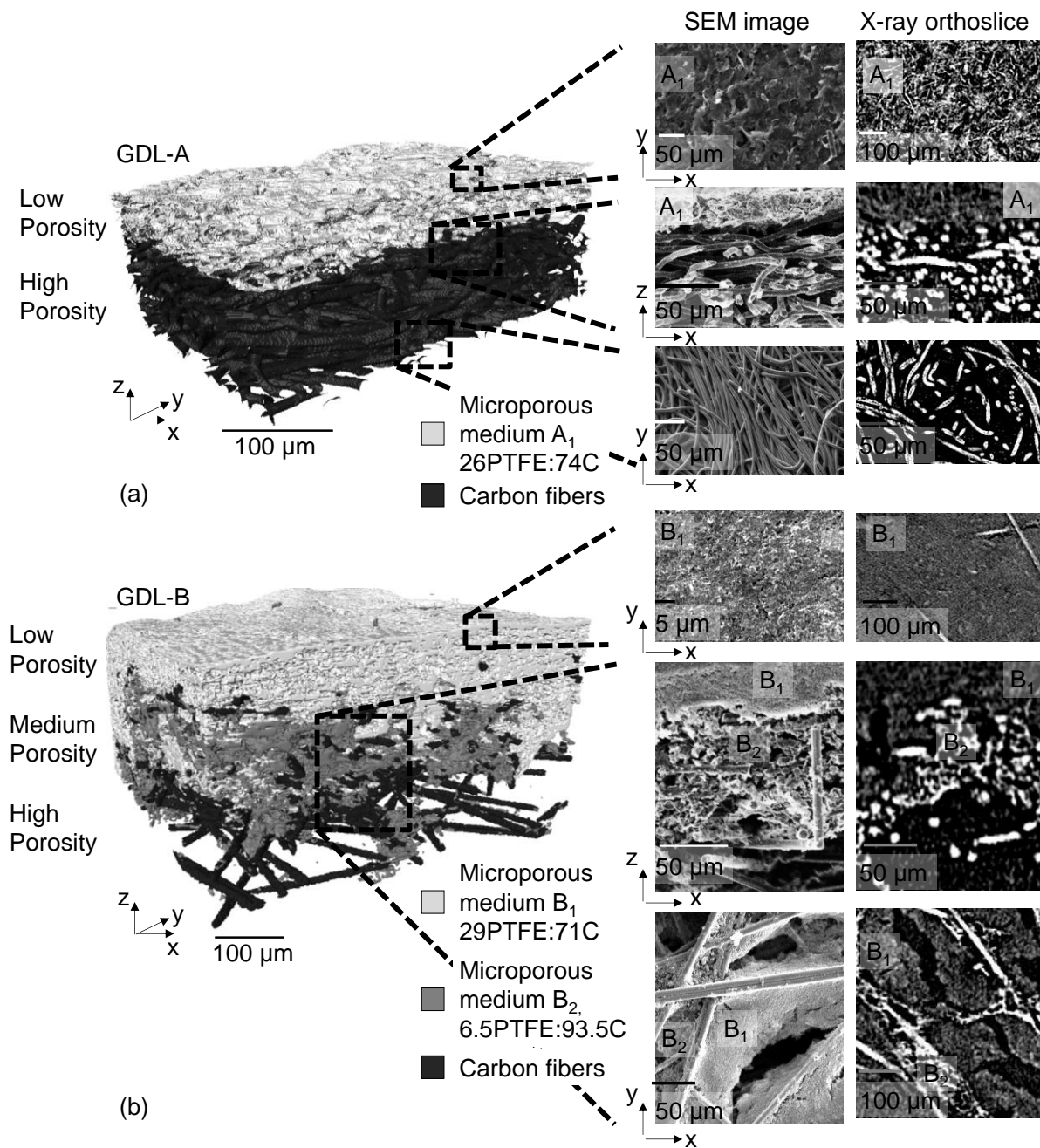
Figure 4. X-ray computed tomography (CT) coupled with SEM of GDL-A (a) and GDL-B (b). X-ray CT of GDL-A and GDL-B are captured with a voxel size of 1.46 μm. The inset images show SEM micrographs of the focused regions marked by black rectangles in the X-ray CT 3D images, alongside X-ray CT orthoslices showing similar features in the same orientation to the SEM data. A_1 describes the low porosity medium of GDL-A, B_1 and B_2 the low and medium porosity media of GDL-B.

Table 1. Carbon-to-fluorine (C-to-F) weight percent, PTFE-to-carbon weight percent and relative porosity regions for GDL-A and GDL-B.

	Material	C / wt %	F / wt%	Pure carbon / wt %	PTFE / wt %	Porosity regions
GDL-A	A_1	80.32	19.68	74.12.1	25.8±2.1	Low
	Fibres	100	0	100	0	High
GDL-B	B_1	78.04	21.96	71.1±2.4	28.8±2.4	Low
	B_2	95.01	4.99	93.4±2.4	6.56±2.4	Medium
	Fibres	100	0	100	0	High

3.2. Fuel cell performance.

3.2.1. Influence of the GDL architecture on the cell voltage.

The two anode GDL types are examined in two, otherwise identical, stacks. Each stack contains two cells to ensure reproducibility and each stack is compressed to the same extent.
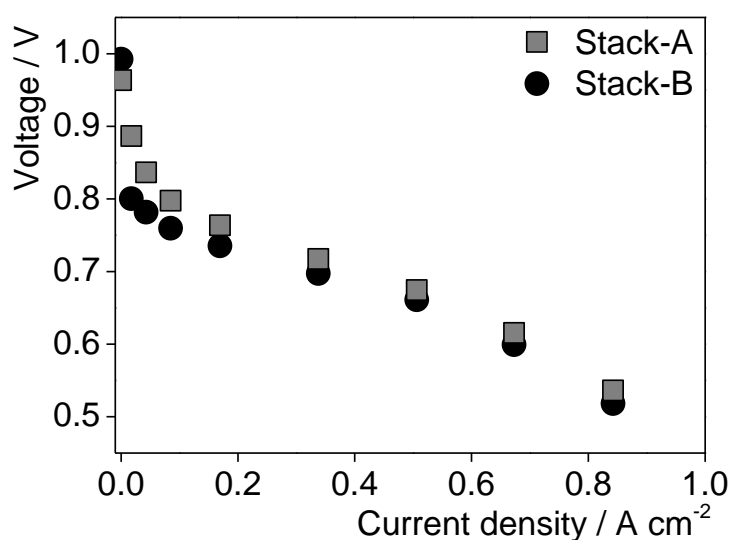

Figure 5. Polarisation curves of Stack-A and Stack-B.

The two stacks have similar performance in the region of typical operation (0.7 V - 0.5 V) (Figure 5). However, Stack-B is systematically lower than Stack-A across the range and particularly at lower current densities. The primary focus of this study relates to the relationship between water distribution, GDL/MPL structure and performance; therefore, operation at current densities higher than 0.4 A cm^{-2}, where water accumulation is likely to occur, will be considered.

3.2.2. Influence of GDL architecture on water distribution.

3.2.2.1.   In-plane water distribution for air cooled open cathode fuel cells.

Using neutron radiography on similar cells, previous imaging work in the through-plane direction showed that the area under the cathode cooling channel lands has the greatest concentration of water [38]. However, as imaging was performed in the through-plane direction, no information was available regarding the distribution of water within the layers of the MEA. In-plane imaging enables the water content of the through the height of the cell to be mapped (z-axis) (Figure 6 a). Given the resolution available (16.5 μm pixel^{-1}), it is not possible to unequivocally identify the membrane, or the catalyst layers, as these are between 1 and 3 pixels (typically 15-50 μm) and therefore not easily accessible using neutron imaging [73], yet cathodic and anodic parts of the cell can be separated. Therefore, the membrane and catalyst layers are represented as a single dashed line on the neutron images, separating the cathode from the anode.

The radiographs highlight here show the hydration of the cell from dry ($t = 0$ s), to partial ($t = 5$ s) and 'full' hydration that represents steady-state operation ($t = 10$ s), once the load is applied (Figure 6). Water is formed at the cathode and initially

accumulates under the cathode cooling channels (t = 5 s). There is no direct water removal mechanism under the cooling channel, so water either diffuses laterally through the GDL to the cathode active channel area where it is evacuated by the large convective flux of air passing through the channel, or back-diffuses to the anode where dry H_2 is flowing. These two mechanisms are highlighted in Figure 6 b, at t = 10 s. Depending on the anode GDL properties and PTFE content, the propensity of water to move back into the anode GDL should be affected. The effect of GDL-A and GDL-B properties is of particular focus in this study.
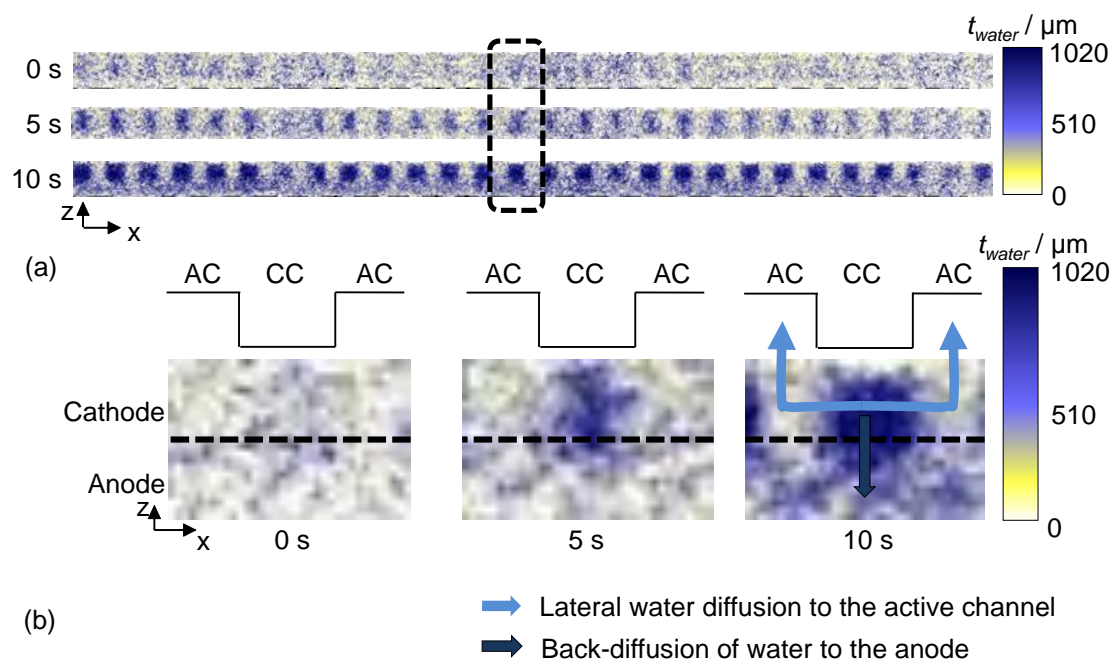

Figure 6. Hydrograph of Stack-B in the in-plane orientation of the fuel cell at 0.5 A cm^{-2} at 0 s, 5 s and 10 s after the load has been applied. Full cell (a), and close-up of the area with dash lines, showing two active channels (AC) and a cooling channel (CC) (b). Pixel size 16.5 μm $\times$ 100 μm (vertical $\times$ horizontal).

3.2.2.2. Comparison between Stack-A and Stack-B.

The comparison between both stacks has been performed in the region of the polarisation where a fuel cell will typically be operated and substantial water

generation occurs (0.5 A cm^{-2} and 0.67 A cm^{-2}). Above 0.7 A cm^{-2}, dehydration of the cell's GDLs due to high temperatures has been shown to occur using combined electro-hydro-thermal analysis [38]. Figure 7 shows a close up view of the water content in the centre of the stack at 0.5 A cm^{-2} and 0.67 A cm^{-2}, for Stack-A (a-c) and Stack-B (b-d). Figure 8 describes the averaged water content for 4 channels at the centre of the stack, with averaging either over the z axis to show the distribution over the x-axis (a), or over the x-axis to show the distribution over the z-axis (b-c). This approach enables to study the gradients.
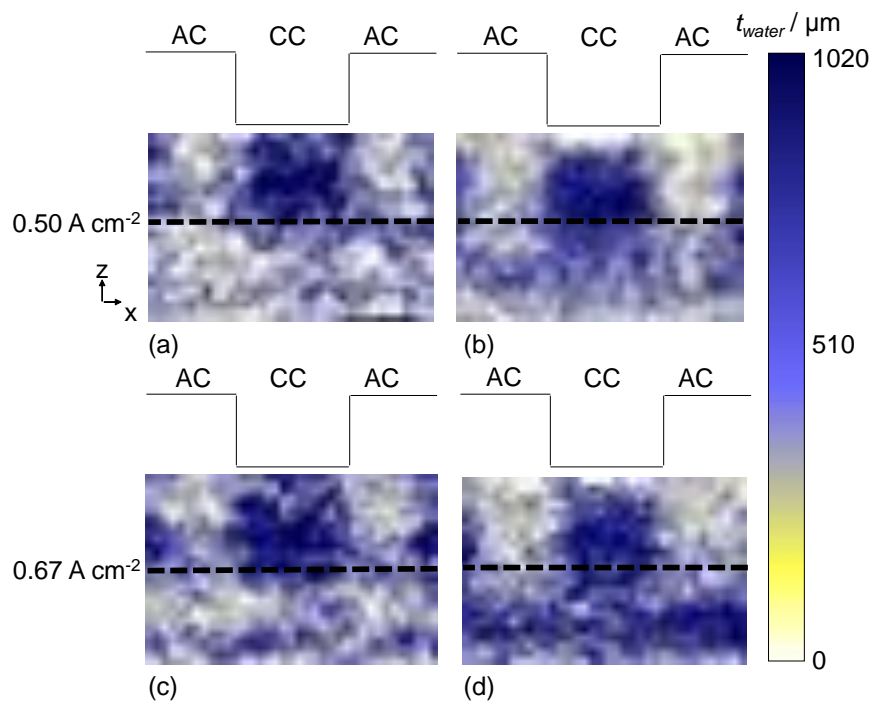

Figure 7. Hydrographs in the centre of the cells, of two active channels (AC) and a cooling channel (CC), located in the same position in the cell, at 0.5 A cm^{-2} and 0.67 A cm^{-2} of Stack-A (a-c) and Stack-B (b-d).

At 0.5 A cm^{-2}, the anode of Stack-A appears relatively dry (Figure 8 b)) and the lateral diffusion of water under the CC land to the AC region, with a drop of water thickness from 1200 μm to 400 μm, can be assumed to be sufficient to remove most of the water from the cathode (Figure 7 a, Figure 8). As the cathode GDL for Stack-B is

18

identical to that of Stack-A, and the same total amount of water is being generated at the cathode (for a given current density), it can be expected that the propensity for lateral diffusion of water through the cathode is the same for both stacks. However, it can be seen that there is less water in the cathode CC and AC regions for Stack-B, with thickness between 1100 μm and 200 μm respectively, i.e. the nature of the anode GDL/MPL is clearly influencing the water distribution in the cathode.

At 0.67 A cm^{-2}, similar features to those at 0.5 A cm^{-2} are observed in the cathode GDL. The water distribution across the cathode, centred about the middle of the CC, is wider for Stack-A, with more water accumulation under the CC and active channel at higher current density for Stack-A (1300 μm and 450 μm), but approximately the same for Stack-B. Much more water is observed in the anode GDL for Stack-B (t_{water}~800 μm), under the AC and CC, whereas it remains dry under the active channel (< ~200μm).

As the load is increased from 0.5 A cm^{-2} to 0.67 A cm^{-2}, the water generation rate through reaction at the cathode increases by 33 %. Upon integrating over the entire cell area, it is revealed that Stack-B ejects less water than Stack-A as the load increase (22.7 % and 16.4% respectively), which is attributed to the different anode GDL/MPL properties.

Table 2. Average water thickness of Stack-A and Stack-B at 0.5 A cm^{-2} and 0.67 A cm^{-2}.

Average water thickness / μm	0.5 A cm^{-2}	0.67 A cm^{-2}	Increase of water content / %
Stack-A	427	497	16.4
Stack-B	370	457	22.7

These differences in distribution are attributed to the structure and properties of GDL-A and GDL-B. GDL-A with the high and uniform PTFE content (26 %), yet low porosity in the microporous layer, forms a water repellent layer which resists back diffusion of water to the anode. On the other hand, for GDL-B, the PTFE gradient from 29 % to 6.5 % in its more distributed (two zone) microporous media of low and medium porosity enables larger amounts of water to be transported through the membrane to the anode.

Considering the MEA profile below the AC, there are several points to note (Figure 7 and 8c). The first is that regardless of the stack / GDL type, there is an approximately linear gradient of water from the GDL/channel interface to the membrane electrolyte. This may be an inherent function of the cathode GDL and air flow rate. Noticeable in Figure 7d (Stack-B) is a feature that shows lower activity of water in the anode MPL under the cathode AC zone. There are two possible explanations for this: (i) the air flux in the cathode acts to dehydrate the anode (diffusion of water from the anode to the cathode) under the AC; or (ii), eventually, at high current density the anode is receiving a lot of water from the cathode under the CC zone, this water is passed to the low PTFE / highly porous fibre region which fills with water and allows lateral diffusion through the fibre pore network, leading to the observed contrast in water activity with the anode MPL under the AC region. Finally, the very thin water layer observed for Stack-A in the anode at 0.67 A cm^{-2} (Figure 8 b-c), may indicate the small proportion of water going through the GDL, despise the PTFE content repelling the majority of it, and slowly accumulating in the porous fibre network.
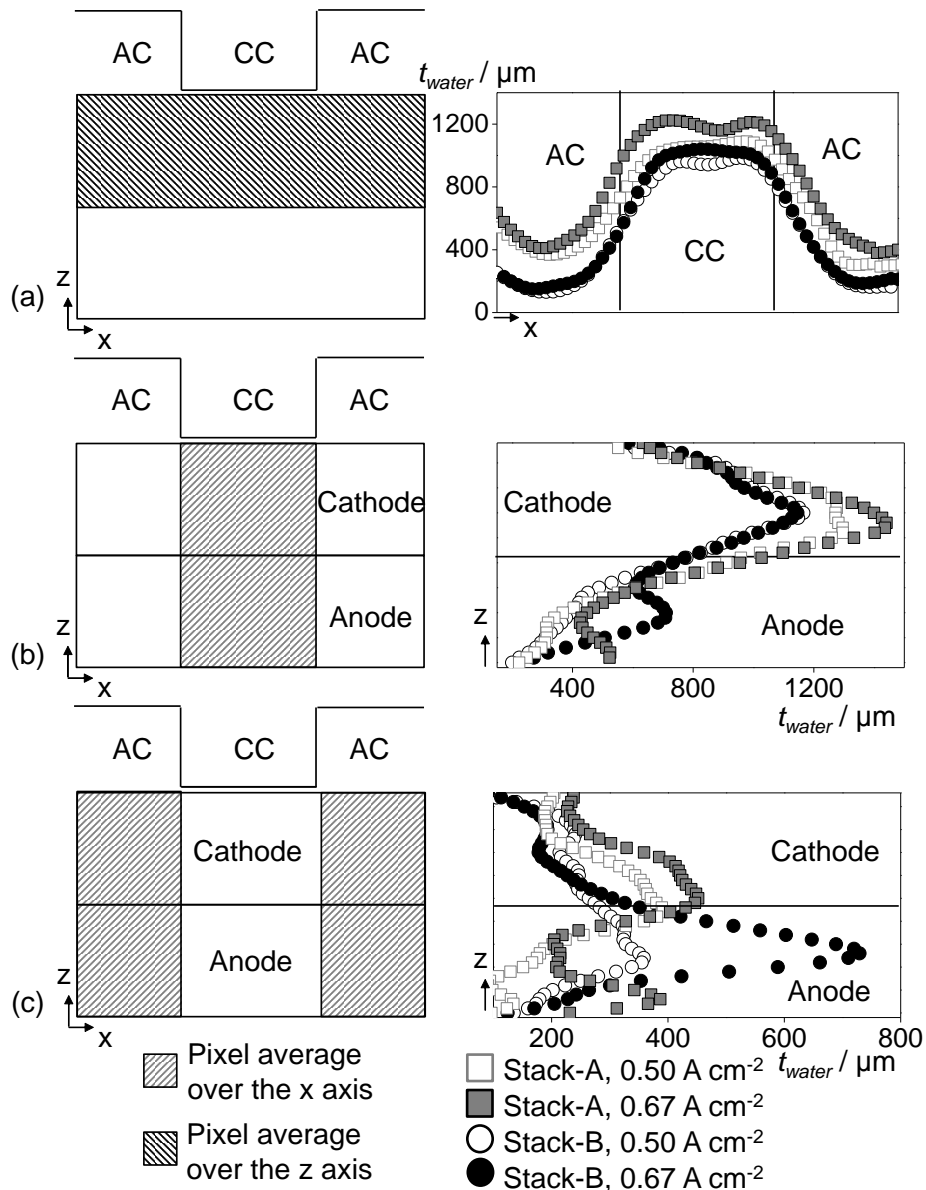
Figure 8. Corresponding water thickness from Figure 7 over 4 central channels; Over the cathode between the active and cooling channels (a), underneath the cooling channel (b) and underneath the active channel (c). AC: active channel, CC: cooling channel.

4. Conclusion

Water plays a critical role in the operation of polymer electrolyte fuel cells. The GDL / MPL are largely responsible for water management and the structure and PTFE

21

content of this component will affect its ability to perform this function. Here, for the first time, the structure and composition of GDLs (determined using TGA, XCT, SEM and EDS) is compared against the in-plane water distribution under operation, determined using neutron radiography.

Two mechanisms for water transport under the cathode cooling channels are identified. The water either diffuses laterally through the cathode GDL to the active channel where the strong convective flux of air removes it from the cell. Alternatively, it diffuses through the membrane to the anode and humidifies the dry hydrogen feed. In practice there will be a combination of these two processes, the properties of the anode GDL influencing the degree to which water diffusion to the anode can take place. High PTFE content, combined with low porosity in the microporous layer (GDL-A) will act as a barrier to water diffusion to the anode. Under these conditions there is a substantially larger amount of water in the cathode AC zone and water egress from the cathode increases. For an anode GDL with a distributed (two zone) MPL with higher porosity, there is a lower barrier to water permeation into the anode, water content at the cathode is lower and under high current densities a significant build-up of water is observed in the anode. In this case there is an increasing the amount of water exiting the stack from the anode.

The analysis presented here, correlating the anode GDL structure with water accumulation through the thickness of the MEA, provides useful insight required for effective MEA / GDL / MPL design. An important message from this work is that when considering water management in PEFCs, the anode and cathode GDL/MPL must be considered collectively using a holistic approach, as one can have a substantial effect on the performance of the other.

5. Acknowledgements

6. References

[1] J.-M. Le Canut, R.M. Abouatallah, D.A. Harrington, Detection of Membrane Drying, Fuel Cell Flooding, and Anode Catalyst Poisoning on PEMFC Stacks by Electrochemical Impedance Spectroscopy, J. Electrochem. Soc. 153 (2006) A857–A864. doi:10.1149/1.2179200.

[2] D. a. McKay, J.B. Siegel, W. Ott, A.G. Stefanopoulou, Parameterization and prediction of temporal fuel cell voltage behavior during flooding and drying conditions, J. Power Sources. 178 (2008) 207–222. doi:10.1016/j.jpowsour.2007.12.031.

[3] H. Li, Y. Tang, Z. Wang, Z. Shi, S. Wu, D. Song, et al., A review of water flooding issues in the proton exchange membrane fuel cell, J. Power Sources. 178 (2008) 103–117. doi:10.1016/j.jpowsour.2007.12.068.

[4] M.W. Reed, R.J. Brodd, Porous Carbon for Fuel Cell Electrodes, Carbon N. Y. 3 (1965) 241–246.

[5] U. Pasaogullari, C.Y. Wang, Liquid Water Transport in Gas Diffusion Layer of Polymer Electrolyte Fuel Cells, J. Electrochem. Soc. 151 (2004) A399. doi:10.1149/1.1646148.

[6] O.S. Burheim, J.G. Pharoah, H. Lampert, P.J.S. Vie, S. Kjelstrup, Through-Plane Thermal Conductivity of PEMFC Porous Transport Layers, J. Fuel Cell Sci. Technol. 8 (2011) 021013. doi:10.1115/1.4002403.

[7] J.P. James, H.-W. Choi, J.G. Pharoah, X-ray computed tomography reconstruction and analysis of polymer electrolyte membrane fuel cell porous transport layers, Int. J. Hydrogen Energy. 37 (2012) 18216–18230. doi:10.1016/j.ijhydene.2012.08.077.

[8] J.-C. Tsai, C.-K. Lin, Effect of PTFE content in gas diffusion layer based on Nafion®/PTFE membrane for low humidity proton exchange membrane fuel cell, J. Taiwan Inst. Chem. Eng. 42 (2011) 945–951. doi:10.1016/j.jtice.2011.05.008.

[9] M.V. Williams, E. Begg, L. Bonville, H.R. Kunz, J.M. Fenton, Characterization of Gas Diffusion Layers for PEMFC, J. Electrochem. Soc. 151 (2004) A1173–1180. doi:10.1149/1.1764779.

[10] S. Park, J.-W. Lee, B.N. Popov, A review of gas diffusion layer in PEM fuel cells: Materials and designs, Int. J. Hydrogen Energy. 37 (2012) 5850–5865. doi:10.1016/j.ijhydene.2011.12.148.

[11] A.Z. Weber, J. Newman, Effects of Microporous Layers in Polymer Electrolyte Fuel Cells, J. Electrochem. Soc. 152 (2005) A677. doi:10.1149/1.1861194.

[12] M. Mortazavi, K. Tajiri, Effect of the PTFE content in the gas diffusion layer on water transport in polymer electrolyte fuel cells (PEFCs), J. Power Sources. 245 (2014) 236–244. doi:10.1016/j.jpowsour.2013.06.138.

[13] E.A. Ticianelli, E.R. Gonzalez, Development and electrochemical studies of gas diffusion electrodes for polymer electrolyte fuel cells, J. Appl. Electrochem. 26 (1996) 297–304.

[14] S. Park, J.W. Lee, B.N. Popov, Effect of PTFE content in microporous layer on water management in PEM fuel cells, J. Power Sources. 177 (2008) 457–463. doi:10.1016/j.jpowsour.2007.11.055.

[15] R.A. Silva, T. Hashimoto, G.E. Thompson, C.M. Rangel, Characterization of MEA degradation for an open air cathode PEM fuel cell, Int. J. Hydrogen Energy. 37 (2012) 7299–7308. doi:10.1016/j.ijhydene.2011.12.110.

[16] T.J. Mason, J. Millichamp, T.P. Neville, A. El-kharouf, B.G. Pollet, D.J.L. Brett, Effect of clamping pressure on ohmic resistance and compression of gas diffusion layers for polymer electrolyte fuel cells, J. Power Sources. 219 (2012) 52–59. doi:10.1016/j.jpowsour.2012.07.021.

[17] S. Odaya, R.K. Phillips, Y. Sharma, J. Bellerive, A.B. Phillion, M. Hoorfar, Electrochimica Acta X-ray Tomographic Analysis of Porosity Distributions in Gas Diffusion Layers of Proton Exchange Membrane Fuel Cells, Electrochim. Acta. 152 (2015) 464–472. doi:10.1016/j.electacta.2014.11.143.

[18] J. Yu, Z. Jiang, M. Hou, D. Liang, Y. Xiao, M. Dou, et al., Analysis of the behavior and degradation in proton exchange membrane fuel cells with a dead-ended anode, J. Power Sources. 246 (2014) 90–94. doi:10.1016/j.jpowsour.2013.06.163.

[19] H. Ostadi, P. Rama, Y. Liu, R. Chen, X.X. Zhang, K. Jiang, 3D reconstruction of a gas diffusion layer and a microporous layer, J. Memb. Sci. 351 (2010) 69–74. doi:10.1016/j.memsci.2010.01.031.

[20] H. Ito, T. Iwamura, S. Someya, T. Munakata, A. Nakano, Y. Heo, et al., Effect of through-plane polytetrafluoroethylene distribution in gas diffusion layers on performance of proton exchange membrane fuel cells, J. Power Sources. 306 (2016) 289–299. doi:10.1016/j.jpowsour.2015.12.020.

[21] A. Pfrang, D. Veyret, F. Sieker, G. Tsotridis, X-ray computed tomography of gas diffusion layers of PEM fuel cells: Calculation of thermal conductivity, Int.

J. Hydrogen Energy. 35 (2010) 3751–3757. doi:10.1016/j.ijhydene.2010.01.085.

[22] F.E. Hizir, S.O. Ural, E.C. Kumbur, M.M. Mench, Characterization of interfacial morphology in polymer electrolyte fuel cells: Micro-porous layer and catalyst layer surfaces, J. Power Sources. 195 (2010) 3463–3471. doi:10.1016/j.jpowsour.2009.11.032.

[23] H. Ostadi, P. Rama, Y. Liu, R. Chen, X.X. Zhang, K. Jiang, Influence of threshold variation on determining the properties of a polymer electrolyte fuel cell gas diffusion layer in X-ray nano-tomography, Chem. Eng. Sci. 65 (2010) 2213–2217. doi:10.1016/j.ces.2009.12.019.

[24] S. Odaya, R.K. Phillips, Y. Sharma, J. Bellerive, a. B. Phillion, M. Hoorfar, X-ray Tomographic Analysis of Porosity Distributions in Gas Diffusion Layers of Proton Exchange Membrane Fuel Cells, Electrochim. Acta. 152 (2015) 464–472. doi:10.1016/j.electacta.2014.11.143.

[25] T. Koido, T. Furusawa, K. Moriyama, An approach to modeling two-phase transport in the gas diffusion layer of a proton exchange membrane fuel cell, J. Power Sources. 175 (2008) 127–136. doi:10.1016/j.jpowsour.2007.09.029.

[26] A. Pfrang, S. Didas, G. Tsotridis, X-ray computed tomography of gas diffusion layers of PEM fuel cells: Segmentation of the microporous layer, J. Power Sources. 235 (2013) 81–86. doi:10.1016/j.jpowsour.2013.01.179.

[27] S. Yu, X. Li, J. Li, S. Liu, W. Lu, Z. Shao, et al., Study on hydrophobicity degradation of gas diffusion layer in proton exchange membrane fuel cells, Energy Convers. Manag. 76 (2013) 301–306. doi:10.1016/j.enconman.2013.07.034.

[28] R.R. Rashapov, J. Unno, J.T. Gostick, Characterization of PEMFC Gas Diffusion Layer Porosity, J. Electrochem. Soc. 162 (2015) F603–F612. doi:10.1149/2.0921506jes.

[29] P. Boillat, D. Kramer, B.C. Seyfang, G. Frei, E. Lehmann, G.G. Scherer, et al., In situ observation of the water distribution across a PEFC using high resolution neutron radiography, Electrochem. Commun. 10 (2008) 546–550. doi:10.1016/j.elecom.2008.01.018.

[30] P. Oberholzer, P. Boillat, R. Siegrist, R. Perego, a. Kästner, E. Lehmann, et al., Cold-Start of a PEFC Visualized with High Resolution Dynamic In-Plane Neutron Imaging, J. Electrochem. Soc. 159 (2012) B235. doi:10.1149/2.085202jes.

[31] H. Murakawa, K. Sugimoto, K. Miyata, H. Asano, N. Takenaka, Y. Saito, Visualization of Water Behavior in the In-plane and Throughplane Directions in a PEFC using a Neutron Image Intensifier, Phys. Procedia. 43 (2013) 277–281. doi:10.1016/j.phpro.2013.03.032.

[32] M. Weiland, P. Boillat, P. Oberholzer, a. Kaestner, E.H. Lehmann, T.J. Schmidt, et al., High resolution neutron imaging for pulsed and constant load operation of passive self-breathing polymer electrolyte fuel cells, Electrochim. Acta. 87 (2013) 567–574. doi:10.1016/j.electacta.2012.09.091.

[33] M.A. Hickner, N.P. Siegel, K.S. Chen, D.S. Hussey, D.L. Jacobson, M. Arif, In Situ High-Resolution Neutron Radiography of Cross-Sectional Liquid Water Profiles in Proton Exchange Membrane Fuel Cells, J. Electrochem. Soc. 155 (2008) B427. doi:10.1149/1.2826287.

[34] A. Iranzo, P. Boillat, P. Oberholzer, J. Guerra, A novel approach coupling neutron imaging and numerical modelling for the analysis of the impact of

water on fuel cell performance, Energy. 68 (2014) 971–981. doi:10.1016/j.energy.2014.03.014.

[35] R. Mukundan, R.L. Borup, Visualising Liquid Water in PEM Fuel Cells Using Neutron Imaging, Fuel Cells. 9 (2009) 499–505. doi:10.1002/fuce.200800050.

[36] R.J. Bellows, M.Y. Lin, M. Arif, A.K. Thompson, D. Jacobson, Neutron Imaging Technique for In Situ Measurement of Water Transport Gradients within Nafion in Polymer Electrolyte Fuel Cells, 146 (1999) 1099–1103.

[37] Quentin Meyer, S. Ashton, S. Torija, C. Gurney, P. Boillat, M. Cochet, et al., Nitrogen Blanketing and Hydrogen Starvation in Dead-Ended-Anode Polymer Electrolyte Fuel Cells Revealed by Hydro-Electro-Thermal Analysis, Electrochim. Acta, Submitt. January 2016. (n.d.).

[38] Q. Meyer, S. Ashton, R. Jervis, D.P. Finegan, P. Boillat, M. Cochet, et al., The Hydro-electro-thermal Performance of Air-cooled, Open-cathode Polymer Electrolyte Fuel Cells: Combined Localised Current Density, Temperature and Water Mapping, Electrochim. Acta. 180 (2015) 307–315. doi:10.1016/j.electacta.2015.08.106.

[39] M.A. Hickner, N.P. Siegel, K.S. Chen, D.N. McBrayer, D.S. Hussey, D.L. Jacobson, et al., Real-Time Imaging of Liquid Water in an Operating Proton Exchange Membrane Fuel Cell, J. Electrochem. Soc. 153 (2006) A902. doi:10.1149/1.2184893.

[40] A. Iranzo, P. Boillat, Liquid water distribution patterns featuring back-diffusion transport in a PEM fuel cell with neutron imaging, Int. J. Hydrogen Energy. 39 (2014) 17240–17245. doi:10.1016/j.ijhydene.2014.08.042.

[41] K. Sugimoto, H. Murakawa, K. Miyata, H. Asano, N. Takenaka, R. Yasuda, Measurement of Water Distribution in through-plane Direction in a PEFC using a Neutron Image Intensifier, Phys. Procedia. 43 (2013) 288–293. doi:10.1016/j.phpro.2013.03.034.

[42] J.P. Owejan, T. a. Trabold, D.L. Jacobson, D.R. Baker, D.S. Hussey, M. Arif, In situ investigation of water transport in an operating PEM fuel cell using neutron radiography: Part 2 – Transient water accumulation in an interdigitated cathode flow field, Int. J. Heat Mass Transf. 49 (2006) 4721–4731. doi:10.1016/j.ijheatmasstransfer.2006.07.004.

[43] P. Stahl, J. Biesdorf, P. Boillat, J. Kraft, K. a. Friedrich, Water Distribution Analysis in the Outer Perimeter Region of Technical PEFC Based on Neutron Radiography, J. Electrochem. Soc. 162 (2015) F677–F685. doi:10.1149/2.0351507jes.

[44] J.B. Siegel, D.A. McKay, A.G. Stefanopoulou, D.S. Hussey, D.L. Jacobson, Measurement of Liquid Water Accumulation in a PEMFC with Dead-Ended Anode, J. Electrochem. Soc. 155 (2008) B1168–B1178. doi:10.1149/1.2976356.

[45] N. Pekula, K. Heller, P. a. Chuang, a. Turhan, M.M. Mench, J.S. Brenizer, et al., Study of water distribution and transport in a polymer electrolyte fuel cell using neutron imaging, Nucl. Instruments Methods Phys. Res. Sect. A Accel. Spectrometers, Detect. Assoc. Equip. 542 (2005) 134–141. doi:10.1016/j.nima.2005.01.090.

[46] D. Kramer, J. Zhang, R. Shimoi, E. Lehmann, A. Wokaun, K. Shinohara, et al., In situ diagnostic of two-phase flow phenomena in polymer electrolyte fuel cells by neutron imaging Part A. Experimental, data treatment, and quantification, Electrochim. Acta. 50 (2005) 2603–2614.

doi:10.1016/j.electacta.2004.11.005.

[47] J. Zhang, D. Kramer, R. Shimoi, Y. Ono, E. Lehmann, A. Wokaun, et al., In situ diagnostic of two-phase flow phenomena in polymer electrolyte fuel cells by neutron imaging, Electrochim. Acta. 51 (2006) 2715–2727. doi:10.1016/j.electacta.2005.08.010.

[48] C. Hartnig, I. Manke, N. Kardjilov, a. Hilger, M. Grünerbel, J. Kaczerowski, et al., Combined neutron radiography and locally resolved current density measurements of operating PEM fuel cells, J. Power Sources. 176 (2008) 452–459. doi:10.1016/j.jpowsour.2007.08.058.

[49] M.A. Hickner, K.S. Chen, N.P. Siegel, Elucidating Liquid Water Distribution and Removal in an Operating Proton Exchange Membrane Fuel Cell via Neutron Radiography, J. Fuel Cell Sci. Technol. 7 (2010) 011001. doi:10.1115/1.3115624.

[50] A. Iranzo, P. Boillat, F. Rosa, Validation of a three dimensional PEM fuel cell CFD model using local liquid water distributions measured with neutron imaging, Int. J. Hydrogen Energy. 39 (2014) 7089–7099. doi:10.1016/j.ijhydene.2014.02.115.

[51] D. Spernjak, S.G. Advani, A.K. Prasad, Simultaneous Neutron and Optical Imaging in PEM Fuel Cells, J. Electrochem. Soc. 156 (2009) B109. doi:10.1149/1.3009585.

[52] H. Iwase, S. Koizumi, H. Iikura, M. Matsubayashi, D. Yamaguchi, Y. Maekawa, et al., A combined method of small-angle neutron scattering and neutron radiography to visualize water in an operating fuel cell over a wide length scale from nano to millimeter, Nucl. Instruments Methods Phys. Res. Sect. A Accel. Spectrometers, Detect. Assoc. Equip. 605 (2009) 95–98. doi:10.1016/j.nima.2009.01.165.

[53] I.A. Schneider, D. Kramer, A. Wokaun, G.G. Scherer, Spatially resolved characterization of PEFCs using simultaneously neutron radiography and locally resolved impedance spectroscopy, Electrochem. Commun. 7 (2005) 1393–1397. doi:10.1016/j.elecom.2005.09.017.

[54] A. Schmitz, M. Tranitz, S. Wagner, R. Hahn, C. Hebling, Planar self-breathing fuel cells, J. Power Sources. 118 (2003) 162–171. doi:10.1016/S0378-7753(03)00080-6.

[55] R. Hahn, S. Wagner, A. Schmitz, H. Reichl, Development of a planar micro fuel cell with thin film and micro patterning technologies, J. Power Sources. 131 (2004) 73–78. doi:10.1016/j.jpowsour.2004.01.015.

[56] S.U. Jeong, E.A. Cho, H.-J. Kim, T.-H. Lim, I.-H. Oh, S.H. Kim, A study on cathode structure and water transport in air-breathing PEM fuel cells, J. Power Sources. 159 (2006) 1089–1094. doi:10.1016/j.jpowsour.2005.12.046.

[57] S.U. Jeong, E.A. Cho, H.-J. Kim, T.-H. Lim, I.-H. Oh, S.H. Kim, Effects of cathode open area and relative humidity on the performance of air-breathing polymer electrolyte membrane fuel cells, J. Power Sources. 158 (2006) 348–353. doi:10.1016/j.jpowsour.2005.09.044.

[58] N. Bussayajarn, H. Ming, K.K. Hoong, W.Y. Ming Stephen, C.S. Hwa, Planar air breathing PEMFC with self-humidifying MEA and open cathode geometry design for portable applications, Int. J. Hydrogen Energy. 34 (2009) 7761–7767. doi:10.1016/j.ijhydene.2009.07.077.

[59] T. Fabian, R. O'Hayre, S. Litster, F.B. Prinz, J.G. Santiago, Passive water management at the cathode of a planar air-breathing proton exchange

membrane fuel cell, J. Power Sources. 195 (2010) 3201–3206. doi:10.1016/j.jpowsour.2009.12.030.

[60] D.T.S. Rosa, D.G. Pinto, V.S. Silva, R.A. Silva, C.M. Rangel, High performance PEMFC stack with open-cathode at ambient pressure and temperature conditions, Int. J. Hydrogen Energy. 32 (2007) 4350–4357. doi:10.1016/j.ijhydene.2007.05.042.

[61] J. Wu, S. Galli, I. Lagana, A. Pozio, G. Monteleone, X. Zi, et al., An air-cooled proton exchange membrane fuel cell with combined oxidant and coolant flow, J. Power Sources. 188 (2009) 199–204. doi:10.1016/j.jpowsour.2008.11.078.

[62] G. Jung, K. Lo, A. Su, F. Weng, C. Tu, T. Yang, et al., Experimental evaluation of an ambient forced-feed air-supply PEM fuel cell, Int. J. Hydrogen Energy. 33 (2008) 2980–2985. doi:10.1016/j.ijhydene.2008.03.056.

[63] A.P. Sasmito, E. Birgersson, K.W. Lum, A.S. Mujumdar, Fan selection and stack design for open-cathode polymer electrolyte fuel cell stacks, Renew. Energy. 37 (2012) 325–332. doi:10.1016/j.renene.2011.06.037.

[64] B. Kim, Y. Lee, A. Woo, Y. Kim, Effects of cathode channel size and operating conditions on the performance of air-blowing PEMFCs, Appl. Energy. 111 (2013) 441–448. doi:10.1016/j.apenergy.2013.04.091.

[65] Q. Meyer, S. Ashton, O. Curnick, T. Reisch, P. Adcock, K. Ronaszegi, et al., Dead-Ended Anode Polymer Electrolyte Fuel Cell Stack Operation Investigated using Electrochemical Impedance Spectroscopy, Off-gas Analysis and Thermal Imaging, J. Power Sources. 254 (2013) 1–9. doi:10.1016/j.jpowsour.2013.11.125.

[66] M. Noorkami, J.B. Robinson, Q. Meyer, O.A. Obeisun, E.S. Fraga, T. Reisch, et al., Effect of temperature uncertainty on polymer electrolyte fuel cell performance5, Int. J. Hydrogen Energy. 39 (2014) 1439–1448.

[67] K. Oates, W.T.W. Potts, Electron beam penetration and X-ray excitation depth in ice, Micron Microsc. Acta. (1984) 1–4.

[68] E.H. Lehmann, P. Vontobel, L. Wiezel, Properties of the radiography facility neutral at SINQ and its potential for use as European reference facility, Nondestruct. Test. Eval. 16 (2001) 191–202. doi:http://dx.doi.org/10.1080/10589750108953075.

[69] P. Boillat, Advanced characterization of polymer electrolyte fuel cells using high resolution neutron imaging, ETH, 2009. doi:10.3929/ethz-a-005911827.

[70] Y. Zhao, H. Yu, D. Xing, W. Lu, Z. Shao, B. Yi, Preparation and characterization of PTFE based composite anion exchange membranes for alkaline fuel cells, J. Memb. Sci. 421-422 (2012) 311–317. doi:10.1016/j.memsci.2012.07.034.

[71] J.A. Conesa, R. Font, Polytetrafluoroethylene Decomposition in Air and Nitrogen, Polym. Eng. Sci. 41 (2001) 2137–2147.

[72] P. Kauranen, A. Pasanen, P. Heikkilä, M. Johansson, J. Pelto, M. Mikkola, et al., Advanced Material Solutions for PEM Fuel Cells – (Phase 2) Final Report, 2010.

[73] B. Smitha, S. Sridhar, A.A. Khan, Solid polymer electrolyte membranes for fuel cell applications - A review, J. Memb. Sci. 259 (2005) 10–26. doi:10.1016/j.memsci.2005.01.035.